Hindawi
International Journal of Antennas and Propagation
Volume 2018, Article ID 6742346, 11 pages
https://doi.org/10.1155/2018/6742346

Research Article

Statistical Characterization of Novel 3D Cluster-Based MIMO Vehicle-to-Vehicle Models for Urban Street Scattering Environments

Xin Chen[1], **Yong Fang**[1], **Yanzan Sun**[1], **Yuntian Pan**[1] and **Weidong Xiang**[2]

[1]*Key Laboratory of Specialty Fiber Optics and Optical Access Networks, Shanghai Institute for Advanced Communication and Data Science, Shanghai University, Shanghai 200444, China*
[2]*Department of Electrical and Computer Engineering, University of Michigan-Dearborn, Dearborn, MI 48128, USA*

Correspondence should be addressed to Xin Chen; chenxin021@shu.edu.cn

Received 26 December 2017; Accepted 3 April 2018; Published 28 June 2018

Academic Editor: Wen-Qin Wang

We develop a novel three-dimensional (3D) cluster-based channel model for vehicle-to-vehicle (V2V) communications under the scenarios of urban street scattering environments. The proposed model combines the flexibility of geometrical channel models with the existing state-of-the-art 3D V2V models. To provide an accurate representation of specific locations and realistic V2V fading environments in a computationally manageable fashion, all clusters are divided into three groups of use cases including "ahead," "between," and "behind" clusters according to the relative locations of clusters. Using the proposed V2V model, we first derive the closed-form expressions of the channel impulse response (CIR), including the line-of-sight (LoS) components and cluster components. Subsequently, for three categories of clusters, the corresponding statistical properties of the reference model are studied. We additionally derive the expressions of the 3D space-time correlation function (STCF), the autocorrelation function (ACF), and 2D STCF. Finally, comparisons with on-road measurement data and numerical experiments demonstrate the validity and effectiveness of the proposed 3D cluster-based V2V model.

1. Introduction

Vehicle-to-vehicle (V2V) communications have received phenomenal attention over the past decade in both commercial and academia domains due to their potential in facilitating the implementation of intelligent transportation systems (ITSs) [1, 2]. With the advent of advanced information and communication technology, enhancing vehicles with accurate V2V models are vital to system design and performance evaluation, which is a necessary next step in the process of vehicle evolution toward autonomous systems. A thorough understanding of the V2V channel is therefore crucial for the development, performance optimization, and test of the present as well as 5G mobile radio systems. In addition, achieving accurate and effective modeling of V2V communication channel has proven to be a challenging task, particularly owing to the diverse and highly dynamic propagation environments. Moreover, vehicular ad hoc network (VANET) research relies heavily on numerical and theoretical simulations, due to the prohibitive costs of deploying real-world measurement campaigns.

Channel modeling is expected to shed light on the real physical attenuation by investigating the channel characteristics, which is critical for developing information-enabled applications to improve traffic safety and mobility [3]. In V2V communication channels, both the transmitter (Tx) and the receiver (Rx) may be in motion and lower than scatterers on surrounding buildings, which is different from conventional fixed-to-mobile (F2M) cellular systems. The performance of V2V propagation channel between Tx and Rx can significantly differ depending on scattering environments around them and whether the link exists line-of-sight (LoS) components owing to buildings, roadside infrastructures, and road bending [4]. V2V channels generally may have contributions from LoS paths, reflections from large stationary and moving objects such as buildings and

neighboring vehicles, and a diffuse base from large numbers of small stationary objects in the environment. To practically analyze and design V2V systems, it is necessary to have the deep knowledge of the underlying propagation channel and the corresponding realistic yet easy-to-use channel model.

There exist several general methods to model the V2V propagation channel, such as geometry-based stochastic models (GBSMs), deterministic models, and stochastic models [1]. In these models, the GBSMs are most widely used in V2V communication systems for theoretical analysis of channel statistics and performance evaluation, which can be classified as regular-shaped GBSMs (RS-GBSMs) [5–10] and irregular-shape GBSMs [11, 12], mainly depending on whether scatterers are located on regular shapes or irregular shapes. The authors of [5–8] presented RS-GBSMs consisting two-ring, two-cylinder, and one ellipse models. However, their underlying assumption of all scatterers is being uniformly distributed on regular geometries, which does not agree with the realistic measurements. In [13, 14], the authors investigated the fixed and moving scatterers on the statistics of MIMO V2V channels under non-line-of-sight (NLoS) scenarios where both the single- and double-bounced components were taken into account, which is more universal in the real-world scattering circumstances. The drawback compared to RS-GBSMs is that closed-form expressions generally cannot be derived, but there are a number of important benefits: the environment can be easily changed and easily reproduce realistic temporal channel variations [12]. In [6, 7], the authors proposed two-dimensional (2D) RS-GBSMs; they neglect signal variations and spatial diversity in the vertical plane. Therefore, 3D two-cylinder and multiring RS-GBSMs were developed for wideband nonisotropic MIMO V2V channels in [8, 9]. Even though many 3D V2V channel models have been proposed over the past few years, they all assumed that the elevation angle and the azimuth angle are completely independent, which also does not adapt to all realistic vehicular scenarios. Moreover, the impact of the distribution of scatterers and moving scatterers on channel statistics was not considered in the existing 3D RS-GBSMs. As for the deterministic models, even though they have shown to agree well with real measurements, they require intensive computations and make it difficult to vary parameters. Stochastic modeling offers a good compromise since it allows reducing the complexity of many physical processes to only a few statistical parameters in a formalism well adapted to the communication engineering community. However, it is based on the wide-sense stationary uncorrelated scattering (WSSUS) assumption, which is usually violated to the nonstationary properties of V2V channels [12, 15].

It is well-known that 3GPP spatial channel model (SCM) is based on empirical measurements and clusters, which models the outdoor scattering environment by a set of discrete reflections [16, 17]. In practical V2V environments, scatterers are intensively distributed in terms of clusters along the roadside since subpaths have similar angle of departure (AoD), angle of arrival (AoA), and latency in a cluster [18–21]. For 3D V2V channel modeling, the conventional 2D models only consider the propagation path in the horizontal plane, which cannot be directly taken into account owing to the elevation angle in 3D space. Furthermore, it is obvious that the previous work in [5–10] is improper because it neglects the impact of the distribution of scattering objects on the channel statistics. A 3D channel modeling study currently under way within 3GPP is expected to shed light on these various issues. In light of this, we present a novel 3D cluster-based MIMO V2V model based on the existing state-of-the-art 2D and 3D scattering channel models. The motivation comes from the fact that both well-known RS-GBSMs and SCM models are aimed at combining the advantages of these two types of models. To the best of our knowledge, there are very few papers that analyze the performance of 3D cluster-based models under vehicular scenarios. Therefore, it is promising that 3D V2V channel modeling is based on clusters but with extensions to catering for V2V modeling requirements and scenarios. In this regard, the major contributions and novelties of this paper are summarized as follows:

(1) We propose a novel 3D cluster-based MIMO V2V channel model under the scenarios of roadside scattering environments. All clusters are classified into three types of clusters according to the relative position of clusters with respect to vehicles (Tx/Rx).

(2) In the proposed model, we present a closed-form expression for channel impulse response (CIR) consisting of LoS components and cluster components. The important channel statistical properties of the reference model are derived and investigated, including 3D space-time correlation function (STCF), autocorrelation function (ACF), and 2D STCF.

(3) The impacts of the locations of clusters, antenna spacings, moving velocities, distributions of scatterers, and the quantity of scattering objects on aforementioned channel statistical properties are investigated. Measurements and extensive simulation results demonstrate the validity and effectiveness of the proposed model. The remainder of this paper is organized as follows. In Section 2, we propose the 3D cluster-based MIMO V2V channel model and derive the expressions of the CIR for LoS paths and cluster paths. The corresponding 3D STCF, ACF, and 2D STCF are developed in Section 3. Numerical analysis and simulations are presented in Section 4, followed by the summary and concluding remarks in Section 5.

2. A Novel 3D Cluster-Based V2V Channel Model

2.1. Description of the Proposed V2V Channel Model. We consider the urban street scattering model as depicted in Figure 1. For ease of comprehension, we redraw the geometrical single-cluster urban street channel model, which constitutes the starting point for the derivation of the proposed model. It is assumed that the cluster lies on the left-hand side of the road, and both Tx and Rx move at a certain speed in the same direction. Between Tx and Rx, there exists a group

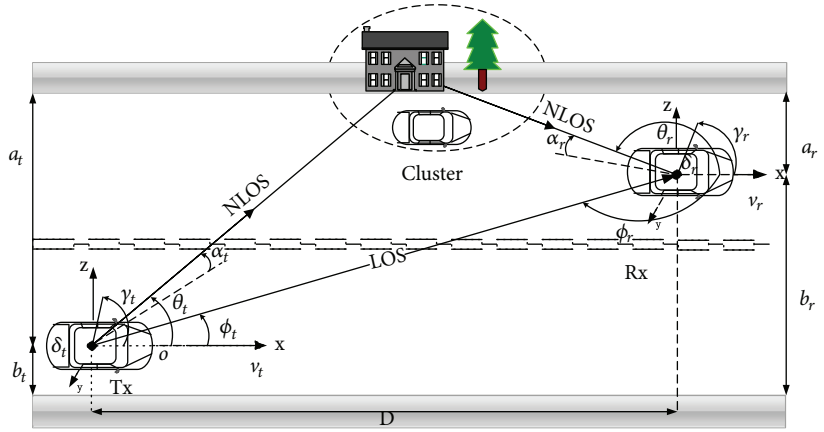

Figure 1: A typical 3D cluster-based V2V scenario.

of dense scatterers, which provide a cluster-based characterization for similar AoD, AoA, and latency and two paths including LoS component and single-bounced cluster component, as illustrated in Figure 1. The Tx/Rx is located at a distance a_t/a_r from the left-hand side of the road and at a distance b_t/b_r from the right-hand side of the road. The distance between Tx and Rx is denoted by D. The transmitter and receiver are equipped with M_t and M_r antenna elements, respectively. The antenna element spacings at Tx and Rx are denoted by δ_t and δ_r, respectively. The angle γ_t/γ_r describes the elevation angle of Tx/Rx linear array antenna. The symbols ϕ_t and ϕ_r are the AoD and AoA of LoS path without any obstruction between Tx and Rx, respectively. The model derives the AoD θ_t and AoA θ_r of the single cluster path, and the symbols α_t and α_r denote the elevation angles of the single cluster path at Tx and Rx, respectively.

The V2V channel model can be described by a temporal channel matrix $\mathbf{H}(t) = [h_{pq}(t)]_{M_t \times M_r}$ of size $M_t \times M_r$, where $p = 1, 2, \ldots, M_t$ and $q = 1, 2, \ldots, M_r$ [16, 22]. Each realisation consists of N clusters composed of M subpaths per cluster. Then, the general expression for CIR $h_{pq}(t)$ between the pth Tx antenna and the qth Rx antenna is generated through a combination of LoS $h_{pq}^{\mathrm{LoS}}(t)$ and cluster component $h_{pq}^{\mathrm{cluster}}(t)$ [23, 24]. The LoS component h_{pq}^{LoS} can be expressed as

$$h_{pq}^{\mathrm{LoS}}(t) = \sqrt{\frac{K_{pq}\Omega_{pq}}{K_{pq}+1}} e^{j\left[2\pi\left(f_T^{\mathrm{LoS}}+f_R^{\mathrm{LoS}}\right)t-(2\pi/\lambda)D_{pq}^{\mathrm{LoS}}\right]}, \quad (1)$$

where

$$\begin{aligned} f_T^{\mathrm{LoS}} &= f_{T,\max}\cos\phi_t, \\ f_R^{\mathrm{LoS}} &= f_{R,\max}\cos\phi_r, \\ D_{pq}^{\mathrm{LoS}} &= D_{T,R} - (M_t - 2p + 1)\frac{\delta_t}{2}\cos\gamma_t \\ &\quad + (M_r - 2q + 1)\frac{\delta_r}{2}\cos\gamma_r, \\ D_{T,R} &= \sqrt{D^2 + (a_t - a_r)^2}. \end{aligned} \quad (2)$$

K_{pq} represents the ratio between the power of the LoS path and the power of clusters (Ricean factor). The symbol Ω_{pq} is the total power between the pth Tx antenna and the qth Rx antenna. The symbols f_T^{LoS} and f_R^{LoS} represent the Doppler shifts of the LoS path due to the movement of Tx and Rx, respectively. $f_{T,\max}$ and $f_{R,\max}$ are the maximum Doppler frequency of Tx and Rx antennas, respectively. D_{pq}^{LoS} denotes the distance between the pth Tx antenna and the qth Rx antenna, while $D_{T,R}$ is the Euclidian distance between Tx and Rx. The cluster component $h_{pq}^{\mathrm{cluster}}(t)$ is given by

$$h_{pq}^{\mathrm{cluster}}(t) = \sqrt{\frac{\Omega_{pq}}{K_{pq}+1}} \lim_{M,N\to\infty} \sum_{n=1}^{N}\sum_{m=1}^{M} \cdot \frac{D^{mn}L_p^{mn}L_q^{mn}e^{j[2\pi(f_T^{mn}+f_R^{mn})t+\varphi_{mn}]}}{\sqrt{MN}}, \quad (3)$$

where

$$\begin{aligned} D^{mn} &= e^{-j(2\pi/\lambda)(a_t/\sin\theta_t^{mn}+a_r/\sin\theta_r^{mn})}, \\ L_p^{mn} &= e^{j\pi(\delta_t/\lambda)(M_t-2p+1)\cos(\theta_t^{mn}-\gamma_t)}, \\ L_q^{mn} &= e^{j\pi(\delta_r/\lambda)(M_r-2q+1)\cos(\theta_r^{mn}-\gamma_r)}, \\ f_T^{mn} &= f_{T,\max}\cos\theta_t^{mn}, \\ f_R^{mn} &= f_{R,\max}\cos\theta_r^{mn}, \end{aligned} \quad (4)$$

where N is the number of clusters and M represents the number of subpaths per cluster. The symbols θ_t^{mn} and θ_r^{mn} are the AoD and AoA of the mth subpath of the nth multipath, respectively. The phases φ_{mn} are independent, identically distributed (iid) random variables, which follow a uniform distribution over the interval $[0, 2\pi)$.

2.2. Clusters Located at Three Different Relative Locations. It has been shown that the V2V radio propagation in scattering environments can be easily influenced by the number and positions of scatterers between Tx and Rx [22]. To evaluate the performance of cluster-based V2V models at specific situations that could occur, we define three categories of clusters according to the relative locations to the transmitter

and the receiver. Figures 2(a)–2(c) depict three cases when clusters are located "ahead," "between," and "behind" with respect to Tx/Rx, respectively, where each position aims at representing a particular type of physical situation, that is, vehicles are approaching, passing, and leaving.

Case 1. Figure 2(a) shows the situation when the cluster is ahead of both Tx and Rx. In this setting, $0 < \theta_t \le \theta_r < \pi/2$; we have

$$\begin{aligned}\widehat{d}_t &= \frac{\sqrt{\widehat{a}^2+\widehat{h}^2}}{\sin\theta_t} = \frac{\widehat{h}}{\sin\alpha_t},\\ \widehat{d}_r &= \frac{\sqrt{\widehat{a}^2+\widehat{h}^2}}{\sin\theta_r} = \frac{\widehat{h}}{\sin\alpha_r}\\ &= \sqrt{\left(\widehat{a}^2+\widehat{h}^2\right)+\left[\left(\widehat{a}^2+\widehat{h}^2\right)\cot\theta_t-1\right]^2},\\ \theta_r &= \tan^{-1}\left[\frac{\sqrt{\widehat{a}^2+\widehat{h}^2}}{\sqrt{\widehat{a}^2+\widehat{h}^2\cot\theta_t-1}}\right].\end{aligned} \tag{5}$$

Here, the hat of the symbol represents the variable in each realization. Therefore,

$$\frac{d\theta_t}{d\theta_r} = \frac{\left[\left(\widehat{a}^2+\widehat{h}^2\right)\cot\theta_t-1\right]^2+\left(\widehat{a}^2+\widehat{h}^2\right)}{\left(\widehat{a}^2+\widehat{h}^2\right)\csc^2\theta_t}. \tag{6}$$

Case 2. Figure 2(b) depicts that the cluster is located between Tx and Rx. In this setting, $0 < \theta_t < \pi/2 \le \theta_r < \pi$; θ_r can be derived from the graph as follows:

$$\theta_r = \pi - \tan^{-1}\left[\frac{\sqrt{\widehat{a}^2+\widehat{h}^2}}{\sqrt{\widehat{a}^2+\widehat{h}^2\cot\theta_t}}\right]. \tag{7}$$

Case 3. Figure 2(c) represents the situation when the cluster is behind both Tx and Rx. In this setting, $\pi/2 \le \theta_t \le \theta_r < \pi$; $\widehat{d}_t$ and $\widehat{d}_r$ have the same expression as in the "ahead" setting.

3. Statistical Characterization of the Cluster-Based V2V Channel Model

3.1. Local 3D STCF. Based on the proposed channel model, the local 3D STCF can be completely determined by the correlation properties of two arbitrary CIRs $h_{pq}(t)$ and $h_{p'q'}(t)$ in the same cluster [23, 24]. Since the LoS and cluster components are independent to each other, and there are no correlations between the underlying processes in different taps, therefore, we have the following local 3D STCF:

$$\begin{aligned}\rho_{h_{pq}(t)h_{p'q'}(t)}(\delta_t,\delta_r,\tau) &\coloneqq \mathbf{E}\left[h^*_{pq}(t)h_{p'q'}(t)(t+\tau)\right]\\ &= \rho^{\mathrm{LoS}}_{pq,p'q'}(\delta_t,\delta_r,\tau)+\rho^{\mathrm{cluster}}_{pq,p'q'}(\delta_t,\delta_r,\tau),\end{aligned} \tag{8}$$

where $\mathbf{E}(\cdot)$ denotes the expectation operator and $(\cdot)^*$ represents the complex conjugate operation. Based on (1), we can obtain the local 3D STCF of the LoS $\rho^{\mathrm{LoS}}_{pq}(\delta_t,\delta_r,\tau)$ as follows:

$$\begin{aligned}\rho^{\mathrm{LoS}}_{pq,p'q'}(\delta_t,\delta_r,\tau) &= \mathbf{E}\left[h^{*\mathrm{LoS}}_{pq}(t)h^{\mathrm{LoS}}_{p'q'}(t+\tau)\right] = \frac{K_{pq}\Omega_{pq}}{K_{pq}+1}e^{j2\pi\left(f^{\mathrm{LoS}}_T+f^{\mathrm{LoS}}_R\right)\tau}e^{j(2\pi/\lambda)\left(D^{\mathrm{LoS}}_{pq}-D^{\mathrm{LoS}}_{p'q'}\right)}\\ &= \frac{K_{pq}\Omega_{pq}}{K_{pq}+1}e^{j2\pi\left(f^{\mathrm{LoS}}_T+f^{\mathrm{LoS}}_R\right)\tau}e^{j(2\pi/\lambda)\left[\delta_t\cos\gamma_t\left(p-p'\right)-\delta_r\cos\gamma_r\left(q-q'\right)\right]},\\ \rho^{\mathrm{cluster}}_{pq,p'q'}(\delta_t,\delta_r,\tau) &\coloneqq \mathbf{E}\left[h^{*\mathrm{cluster}}_{pq}(t)h^{\mathrm{cluster}}_{p'q'}(t+\tau)\right]\\ &= \frac{\Omega_{pq}}{K_{pq}+1}\sum_{n=1}^{N}\sum_{m=1}^{M}\frac{L^{mn}_{pp'}(\delta_t,\theta^{mn}_t)L^{mn}_{qq'}(\delta_r,\theta^{mn}_r)e^{j2\pi\left(f^{mn}_T(\theta^{mn}_t)+f^{mn}_R(g(\theta^{mn}_t))\right)\tau}}{MN},\end{aligned} \tag{9}$$

where

$$L^{mn}_{pp'}(\delta_t,\theta^{mn}_t) = e^{j2\pi(\delta_t/\lambda)\cos\left(\theta^{mn}_t-\gamma_t\right)\left(p-p'\right)}, \tag{10}$$

$$L^{mn}_{qq'}(\delta_r,\theta^{mn}_r) = e^{j2\pi(\delta_r/\lambda)\cos\left(\theta^{mn}_r-\gamma_r\right)\left(q-q'\right)}, \tag{11}$$

$$f^{mn}_T(\theta^{mn}_t) = f_{T,\max}\cos\theta^{mn}_t, \tag{12}$$

$$f^{mn}_R(g(\theta^{mn}_t)) = f_{R,\max}\cos(g(\theta^{mn}_t)). \tag{13}$$

The function $g(\cdot)$ expresses the relationship between AoD θ^{mn}_t and AoA θ^{mn}_r, which can be calculated from Figure 3 as

$$g(\theta^{mn}_t) = \arccos\left[\frac{d_t\cos(\theta^{mn}_t)-D_{T,R}}{d_r}\right]. \tag{14}$$

It is noteworthy that the AoD θ^{mn}_t and AoA θ^{mn}_r are dependent from Figure 2, while the contribution of the LoS

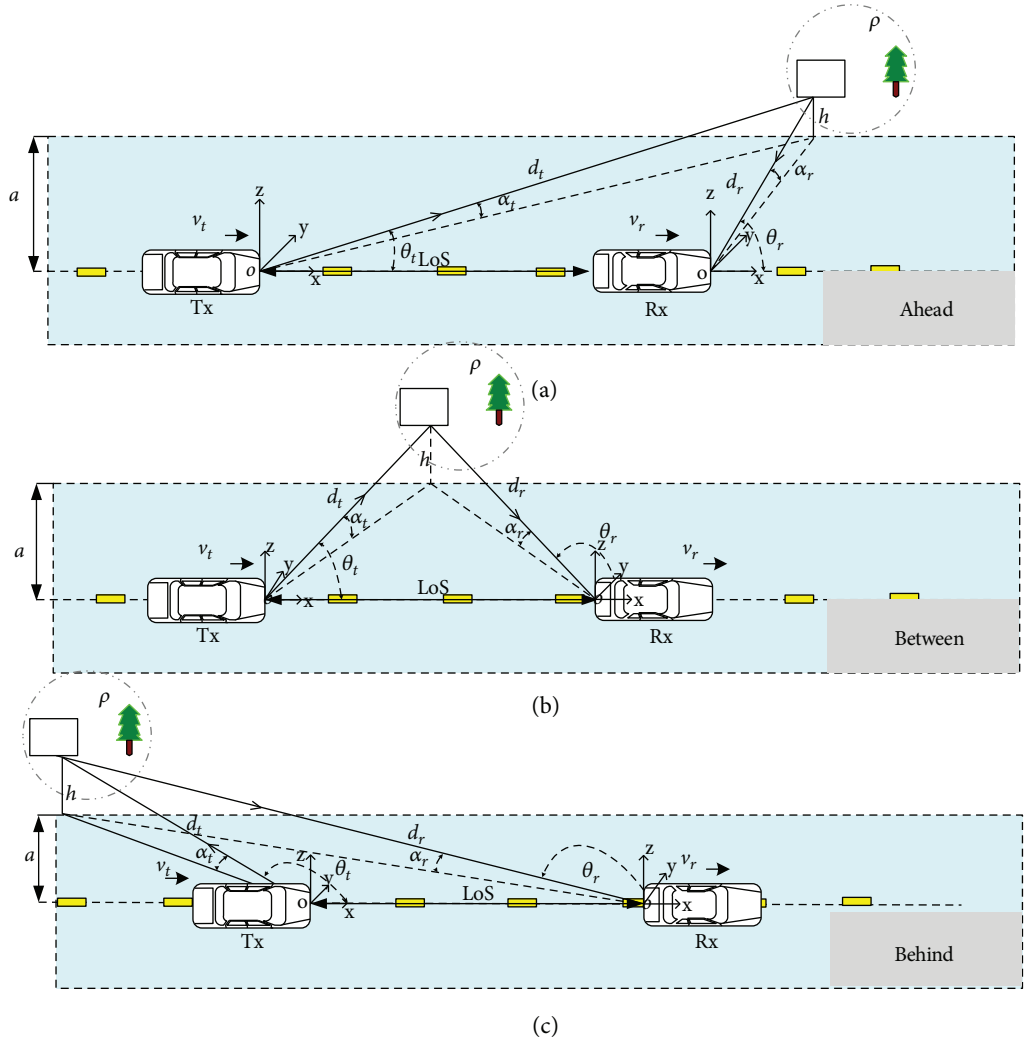

Figure 2: Three locations of clusters with respect to Tx and Rx (Note that v_t and v_r denote the speed of Tx and Rx, respectively; d_t and d_r are the distance between clusters and Tx/Rx antenna elements, respectively; ρ and h are the density and average height of clusters, respectively; and the symbol a is the average distance from vehicles Tx/Rx to the left/right roadside.)

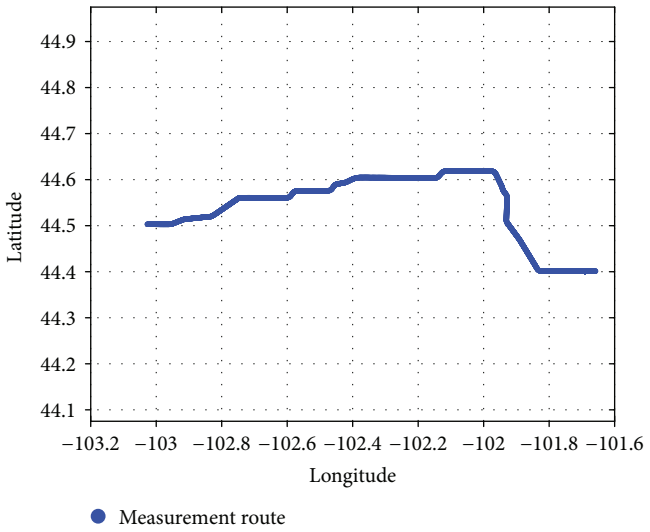

Figure 3: The measurement GPS track in South Dakota, USA (N: 44°40′13″~44°50′30″, W: −101°65′82″~−103°02′72″).

component in multiple clusters is independent of the number of clusters M. In light of this, the $\rho^{\text{cluster}}_{pq,p'q'}(\delta_t, \delta_r, \tau)$ can be defined as

$$\rho^{\text{cluster}}_{pq,p'q'}(\delta_t, \delta_r, \tau) = \rho^{\text{ahead}}_{pq,p'q'}(\delta_t, \delta_r, \tau) + \rho^{\text{between}}_{pq,p'q'}(\delta_t, \delta_r, \tau) + \rho^{\text{behind}}_{pq,p'q'}(\delta_t, \delta_r, \tau), \tag{15}$$

where

$$\rho^{\text{ahead}}_{pq,p'q'}(\delta_t, \delta_r, \tau) = \frac{\Omega_{pq}}{K_{pq}+1} \int_0^{\pi/2} L^{mn}_{pp'}(\delta_t, \theta^{mn}_t) L^{mn}_{qq'} \cdot (\delta_t, g(\theta^{mn}_t)) e^{j2\pi[f^{mn}_T(\theta^{mn}_t) + f^{mn}_R(g(\theta^{mn}_t))]\tau} \cdot p(\theta^{mn}_t) d\theta^{mn}_t. \tag{16}$$

In (13), the probability density function for the AoD θ^{mn}_t is denoted by $p(\theta^{mn}_t)$, which follows the stochastic distribution over three intervals in Figures 3(a)–3(c), respectively.

For the sake of brevity, the expressions of $p^{\text{between}}_{pq,p'q'}(\delta_t, \delta_r, \tau)$ and $p^{\text{behind}}_{pq,p'q'}(\delta_t, \delta_r, \tau)$ are omitted here.

3.2. ACF. The ACF $r_{h_{pq}}(\tau)$ of the complex channel gain $h_{pq}(t)$ can be determined by using the definition $r_{h_{pq}}(\tau) \coloneqq \mathbf{E}\{h^*_{pq}(t)h_{pq}(t+\tau)\}$ in which $\mathbf{E}\{\cdot\}$ denotes the expectation operator. The ACF $r_{h_{pq}}(\tau)$ can be deduced from the 3D STCF $\rho_{h_{pq}(t)h_{p'q'}(t)}(\delta_t, \delta_r, \tau)$ by setting the antenna element spacing δ_t and δ_r to zero [24]. Thus,

$$\begin{aligned} r_{h_{pq}}(\tau) &= \rho_{h_{pq}(t)h_{p'q'}(t)}(0,0,\tau) \\ &= \rho^{\text{LoS}}_{pq,p'q'}(0,0,\tau) + \rho^{\text{cluster}}_{pq,p'q'}(0,0,\tau) \\ &= \frac{K_{pq}\Omega_{pq}}{K_{pq}+1} e^{j2\pi\left(f^{\text{LoS}}_T + f^{\text{LoS}}_R\right)\tau} \\ &\quad + \frac{\Omega_{pq}}{K_{pq}+1}\int_0^{\pi} e^{j2\pi\left[f^{mn}_T(\theta^{mn}_t) + f^{mn}_R(g(\theta^{mn}_t))\right]\tau} p(\theta^{mn}_t)\, d\theta^{mn}_t. \end{aligned} \tag{17}$$

Worth pointing out is that 2D STCF $\rho_{h_{pq}(t)h_{p'q'}(t)}(\delta_t, \delta_r)$ can also be deduced from 3D STCF $\rho_{h_{pq}(t)h_{p'q'}(t)}(\delta_t, \delta_r, \tau)$ by setting τ to zero. Thus,

$$\begin{aligned} r_{h_{pq}}(\tau) &= \rho_{h_{pq}(t)h_{p'q'}(t)}(\delta_t, \delta_r, 0) \\ &= \rho^{\text{LoS}}_{pq,p'q'}(\delta_t, \delta_r, 0) + \rho^{\text{cluster}}_{pq,p'q'}(\delta_t, \delta_r, 0), \end{aligned} \tag{18}$$

where

$$\begin{aligned} \rho^{\text{LoS}}_{pq,p'q'}(\delta_t, \delta_r, 0) &= \frac{K_{pq}\Omega_{pq}}{K_{pq}+1} e^{j(2\pi/\lambda)\left[\delta_t \cos\gamma_t(p-p') - \delta_r \cos\gamma_r(q-q')\right]}, \\ \rho^{\text{cluster}}_{pq,p'q'}(\delta_t, \delta_r, 0) &= \frac{\Omega_{pq}}{K_{pq}+1}\int_0^{\pi} L^{mn}_{pp'}(\delta_t, \theta^{mn}_t) L^{mn}_{qq'} \\ &\quad \cdot (\delta_t, g(\theta^{mn}_t)) p(\theta^{mn}_t)\, d\theta^{mn}_t. \end{aligned} \tag{19}$$

4. Numerical Results

4.1. Simulation Parameters. This section presents results obtained by evaluating the CIR for the NLoS propagation conditions. The proposed cluster-based V2V channel model is validated by measurements conducted at 5.9 GHz, with a bandwidth of 75 MHz using a transmit power of 27 dBm. The speed and separation distance of Tx and Rx were obtained from GPS records in SD 34 Highway, South Dakota, USA. The snapshot repetition time was set to $t_s = 300\,\mu$s. The measurement GPS track is shown in Figure 3. This measurement was taken near the rush hour with heavy traffic density. Each realisation consists of three clusters composed of 20 effective subpaths per cluster. In our V2V model simulation, some key parameters are generated according to measurement campaigns. The Ricean factor K_{pq} and the total power Ω_{pq} are set to two and one, respectively. The rest

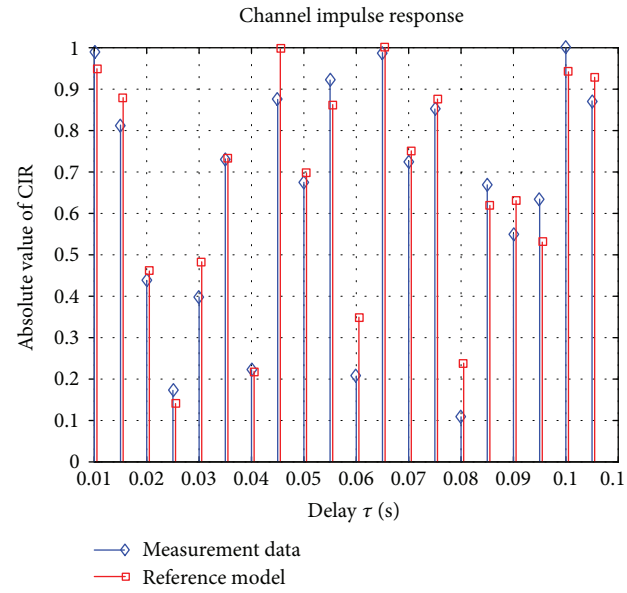

Figure 4: Power-delay profile of the channel for low moving speed of vehicles (Tx/Rx): $v_t = v_r = 20$ km/h.

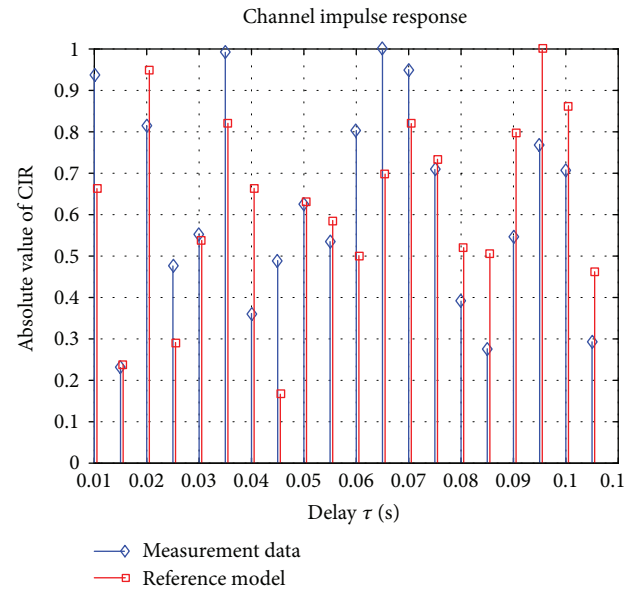

Figure 5: Power-delay profile of the channel for high moving speed of vehicles (Tx/Rx): $v_t = v_r = 80$ km/h.

of parameters have been chosen as follows: $D = 200$ m, $f_{T,\max} = f_{R,\max} = 95.6$ Hz, and $\delta_t = \delta_r = \lambda$. For subpaths of a cluster, the AoD θ^{mn}_t and AoA θ^{mn}_r are stochastically distributed at the center of the cluster angle over these three regions: (i) "ahead" cluster central angles $\theta_t = 31.5^\circ$ and $\theta_r = 66.3^\circ$, (ii) "between" cluster central angles $\theta_t = 35.6^\circ$ and $\theta_r = 126.8^\circ$, and (iii) "behind" cluster central angles $\theta_t = 110.6^\circ$ and $\theta_r = 162.5^\circ$, where the standard deviations are less than one degree. Considering the angles of subpaths in a cluster within the relative azimuth offsets ($\Delta\theta_t \le 1^\circ$, $\Delta\theta_r \le 1^\circ$) with respect to their neighboring subpaths, the radius of each cluster is 10 m and is independent with

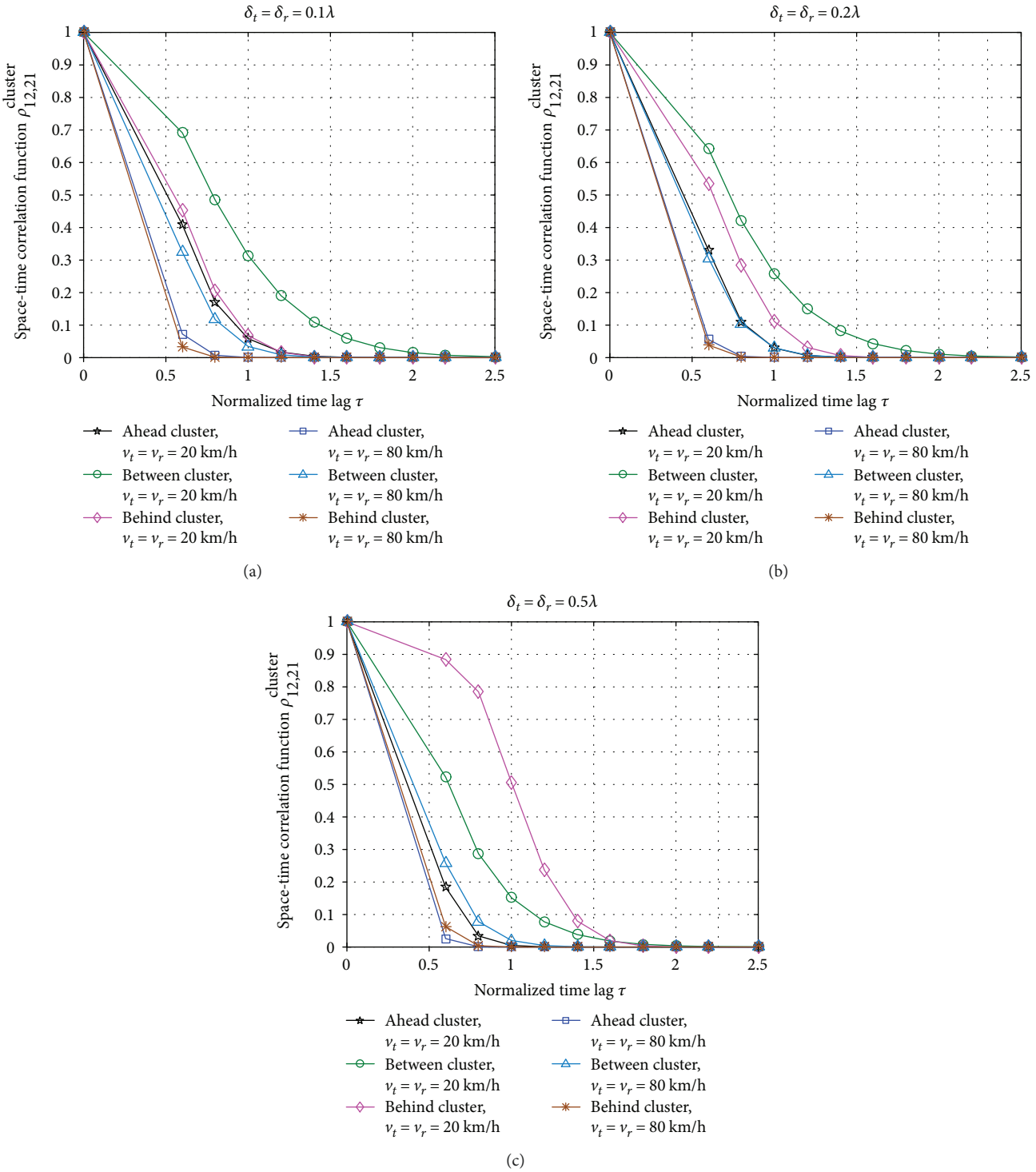

FIGURE 6: The absolute value of the 3D STCF $\rho^{\text{cluster}}_{12,21}$ of the reference model under different antenna element spacings.

other two clusters. Both Tx and Rx move at the speed of 20/80 (km/h) in the same direction.

4.2. CIR of the V2V Channel. To validate the accuracy of the proposed V2V channel model, we have compared the CIR of the reference model with realistic V2V channel measurements. The propagation environment encompasses three clusters located on the left-hand side of the road. A good fitting between the CIR of the simulation model and measurements can be observed in Figure 4, which demonstrated the effectiveness of the proposed model. By comparing Figures 4 and 5, we can observe that the gap of the CIR between measurement data and the reference model becomes bigger by increasing the speed of vehicles (Tx/Rx) from

Table 1: Environment parameters.

Channel scenario	Case 1: ahead cluster	Case 2: between cluster	Case 3: behind cluster
Number of antennas at Tx/Rx	$M_t = M_r = 2$	$M_t = M_r = 2$	$M_t = M_r = 2$
Number of clusters	$N = 1/5/10$	$N = 1/5/10$	$N = 1/5/10$
Number of subpaths per cluster	$M = 20$	$M = 20$	$M = 20$
Antenna element spacing	$\delta_t = \delta_r = 0.1/0.2/0.5\ \lambda$	$\delta_t = \delta_r = 0.1/0.2/0.5\ \lambda$	$\delta_t = \delta_r = 0.1/0.2/0.5\ \lambda$
Maximum Doppler frequency	$f_{T,\max} = f_{R,\max} = 109$ Hz /410 Hz	$f_{T,\max} = f_{R,\max} = 109$ Hz /410 Hz	$f_{T,\max} = f_{R,\max} = 109$ Hz /410 Hz
Distance between Tx and Rx	200 m	200 m	200 m
Distance between clusters and Tx/Rx antenna elements	$d_t = 120$ m, $d_r = 30$ m	$d_t = 80$ m, $d_r = 70$ m	$d_t = 20$ m, $d_r = 130$ m
Distance from vehicles to the left-/right-hand roadside	$a_t/a_r = b_t/b_r = 10$ m	$a_t/a_r = b_t/b_r = 10$ m	$a_t/a_r = b_t/b_r = 10$ m
AoD of the central cluster	$\theta_t = 30^\circ$	$\theta_t = 60^\circ$	$\theta_t = 120^\circ$
AoA of the central cluster	$\theta_r = 60^\circ$	$\theta_r = 120^\circ$	$\theta_r = 150^\circ$
Elevation angles of clusters at Tx/Rx	$\alpha_t = \alpha_r = 30^\circ$	$\alpha_t = \alpha_r = 30^\circ$	$\alpha_t = \alpha_r = 30^\circ$
Velocity of vehicles	$v_t = v_r = 20/80$ (km/h)	$v_t = v_r = 20/80$ (km/h)	$v_t = v_r = 20/80$ (km/h)
Distribution of scatterers	Uniform/stochastic	Uniform/stochastic	Uniform/stochastic

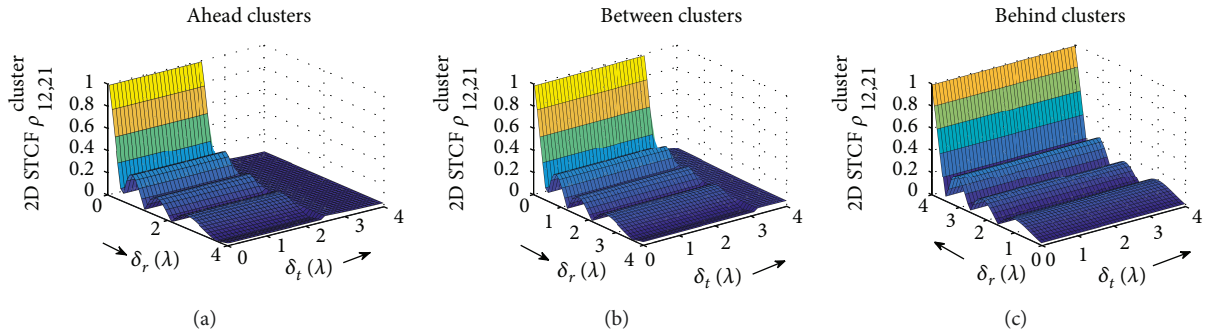

Figure 7: The absolute value of the 2D STCF $\rho^{\text{cluster}}_{12,21}$ of the reference model under NLoS conditions ($K = 0$).

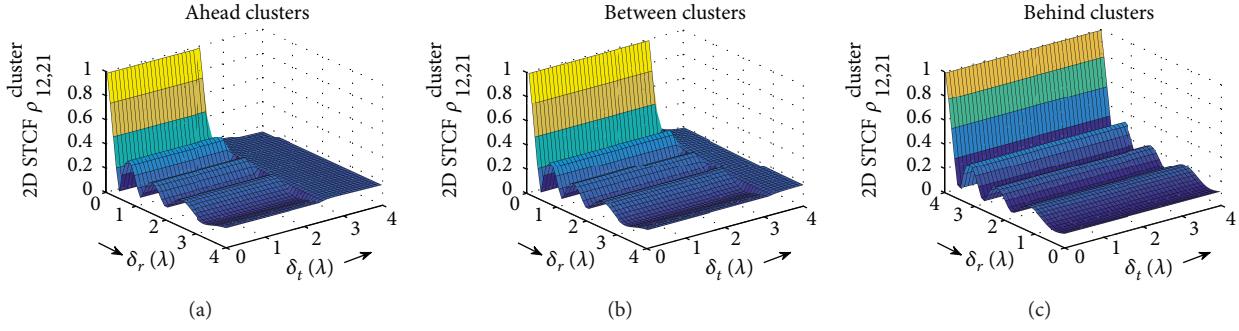

Figure 8: The absolute value of the 2D STCF $\rho^{\text{cluster}}_{12,21}$ of the reference model under LoS conditions ($K = 2$).

20 km/h to 80 km/h. Accordingly, the standard variance between the reference model and on-road measurement data rises from 0.0047 in Figure 4 to 0.0195 in Figure 5. This fact can be attributed to the great change of Doppler spreads and angular variations as the increase of vehicular speed becomes more dynamic. In this regard, Figures 4 and 5 have proved that high velocity of vehicles has a major impact on the CIR curve of the V2V channel.

4.3. STCF of the Proposed V2V Model. Numerical results obtained for the 3D STCF are shown in Figure 6. The key parameters of simulations are summarized in Table 1.

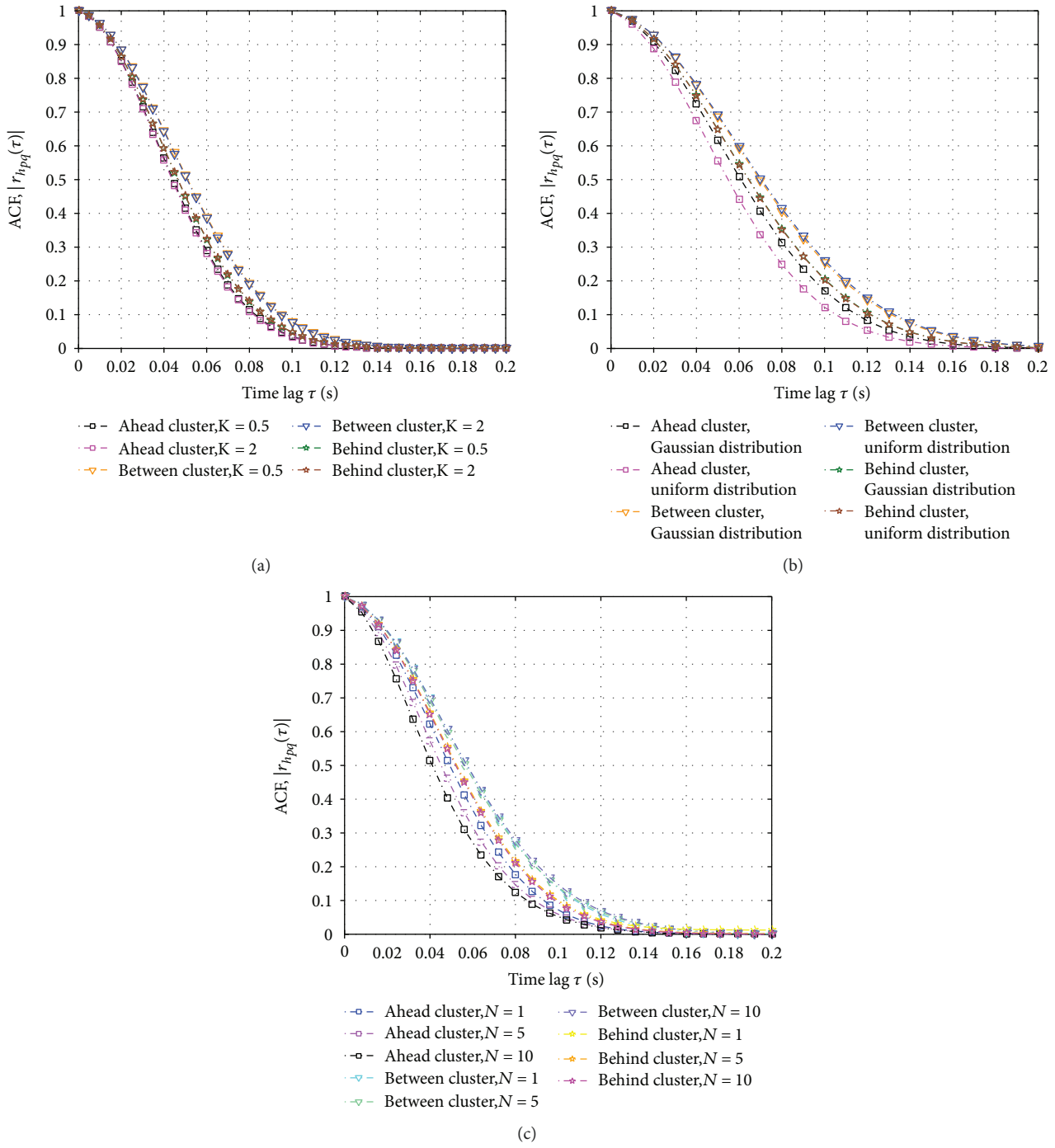

FIGURE 9: The absolute value of the ACF $r_{h_{pq}}(\tau)$ of the reference model under (a) different Ricean factors K, different distributions of scatterers and different number of clusters over three locations.

Figures 6(a)–6(c) present the impact of antenna element spacings, moving speeds, and positions of clusters on the STCF. As we can see in Figure 6(a), the coherence time of the proposed channel decreases as the speed of Tx/Rx from 20 km/h to 80 km/h. In other words, the STCF in high moving scenario is fading faster than that in low moving scenario. Specially, the variations of coherence time reduce by 0.6, 0.8, and 0.8 time lags for "ahead," "between," and "behind" clusters, respectively. A similar behavior can also be observed in Figures 6(b) and 6(c). Moreover, the coherence time of "ahead" clusters and "between" clusters decreases as antenna element spacings δ_t and δ_r increase form 0.1 λ to 0.5 λ, but there is a rise for "behind" clusters in low moving scenario. This is due to the assumption of the angles of "behind" clusters ($\pi/2 \le \theta_t \le \theta_r < \pi$), which shows a negative correlation when both AoD and AoA exceed $\pi/2$. It is obvious that the position of scatterers greatly affects the STCF of the V2V channel at different moving conditions.

Figure 7 depicts the 2D STCF $\rho_{12,21}^{\text{cluster}}$ for three locations of clusters. Here, we consider the NLoS situations, where each scenario contains five stochastic clusters over the corresponding regions in Figure 2. The rest of key parameters are described in Table 1. It is noteworthy that both the locations of clusters and velocities of the transmitter/receiver have no influence on the envelope of 2D STCF. Under NLoS propagation environments, the curves of 2D STCF decrease as the antenna spacing increases. Comparing with Figures 7(a)–7(c), the absolute values of $\rho_{12,21}^{\text{cluster}}$ for "ahead" clusters and "between" clusters have dropped to near zero when the TX antenna spacing δ_t exceeds a critical value 3λ. In Figure 8, we illustrate the influence of the LoS component on the 2D STCF $\rho_{12,21}^{\text{cluster}}$. The simulation results of Figure 8 are obtained by setting the Ricean factor $K = 2$. Observing from Figures 7 and 8, the absolute value of local 2D STCF increases a little in Figure 8, which indicates that the correlation increases as we increase the Ricean factor K. However, there is no great influence on the overall curve of local 2D STCF.

4.4. ACF of the V2V Channel. Numerical results obtained for the ACF $r_{h_{pq}}(\tau)$ are shown in Figure 9. Both Tx and Rx are moving in the same direction. To study the influence of the Ricean factor K, distributions of scatterers, and quantity of clusters over three different regions on the temporal ACF $r_{h_{pq}}(\tau)$, we keep the same propagation environments as shown in Table 1. From Figure 9(a), it can be seen that the Ricean factor does not influence significantly the curvature of the ACF. A good fitting between $K = 0.5$ and $K = 2$ of "ahead," "between," and "behind" clusters can be observed in Figure 9(a). Figure 9(b) shows the simulation results of the influence of the truncated Gaussian distribution and uniform distribution of scatterers over the regions of "ahead" clusters, "between" clusters, and "behind" clusters. A good fitting between the truncated Gaussian distribution and uniform distribution of the "between" clusters and "behind" clusters can also be observed in Figure 9(b), while the distribution of scatterers for "ahead" clusters has a stronger correlation with the ACF than those of other two types of clusters. In addition, similar situation can also be adapted to the influence of the quantity of clusters on the ACF in Figure 9(c). Over these three regions, the ACF of "ahead" clusters can be easily influenced by the number of clusters and distributions of scattering objects.

5. Conclusion

In this paper, a novel 3D cluster-based MIMO V2V model has been proposed for street scattering environments.

In this model, three categories of clusters are classified to characterize near-field effects of scatterers, resulting in CIR, AoD and AoA statistics, and antenna spacing, mobility, and position variations on the STCF and ACF. It has also demonstrated that high moving conditions have great impact on the CIR of the V2V channel. It is evident that the antenna element spacing increases from 0.1λ to 0.5λ, resulting in a rise for the coherence time of behind clusters in low moving environments. Additionally, under the NLoS situations, the envelope of 2D STCF cannot be easily influenced by the position of clusters and the speed of Tx/Rx. Furthermore, the absolute value $\rho_{pq,p'q'}^{\text{cluster}}$ of "ahead" and "between" clusters gradually drops to near zero when the Tx antenna spacing δ_t exceeds a critical value 3λ. The ACF of "ahead" clusters is more susceptible to the number and distribution of clusters, which validates the impact of three types of clusters on the proposed 3D V2V channel model. For future work, we intend to consider the time-varying angles and the effect of moving scatterers in this model. Moreover, massive MIMO and birth-death clusters can be employed in future extensions of the V2V channel model.

Conflicts of Interest

The authors declare that they have no conflicts of interest.

Acknowledgments

The work is supported by the National Natural Science Foundation of China under Grant nos. 61673253, 61271213, and 61501289 and the Specialized Research Fund for the Doctoral Program of Higher Education of China under Grant no. 20133108110014. This work is also supported by the China Scholarship Council (CSC), and the authors would like to thank the staff of Vehicle Electronics Laboratory at University of Michigan-Dearborn, USA, for providing good suggestions of V2V channel modeling.

References

[1] D. W. Matolak, "Channel modeling for vehicle-to-vehicle communications," *IEEE Communications Magazine*, vol. 46, no. 5, pp. 76–83, 2008.

[2] E. Uhlemann, "Continued dispute on preferred vehicle-to-vehicle technologies [connected vehicles]," *IEEE Vehicular Technology Magazine*, vol. 12, no. 3, pp. 17–20, 2017.

[3] Y. Yuan, C. X. Wang, Y. He, M. M. Alwakeel, and H. M. Aggoune, "3D wideband non-stationary geometry-based stochastic models for non-isotropic MIMO vehicle-to-vehicle channels," *IEEE Transactions on Wireless Communications*, vol. 14, no. 12, pp. 6883–6895, 2015.

[4] M. Riaz, N. M. Khan, and S. J. Nawaz, "A generalized 3-D scattering channel model for spatiotemporal statistics in mobile-to-mobile communication environment," *IEEE Transactions on Vehicular Technology*, vol. 64, no. 10, pp. 4399–4410, 2015.

[5] X. Zhao, X. Liang, S. Li, and K. Haneda, "Mobile-to-mobile wideband MIMO channel realization by using a two-ring geometry-based stochastic scattering model," *Wireless Personal Communications*, vol. 84, no. 4, pp. 2445–2465, 2015.

[6] L. Cheng, D. D. Stancil, and F. Bai, "A roadside scattering model for the vehicle-to-vehicle communication channel," *IEEE Journal on Selected Areas in Communications*, vol. 31, no. 9, pp. 449–459, 2013.

[7] R. B. Ertel and J. H. Reed, "Angle and time of arrival statistics for circular and elliptical scattering models," *IEEE Journal on Selected Areas in Communications*, vol. 17, no. 11, pp. 1829–1840, 1999.

[8] X. Zhao, X. Liang, S. Li, and B. Ai, "Two-cylinder and multi-ring GBSSM for realizing and modeling of vehicle-to-vehicle wideband MIMO channels," *IEEE Transactions on Intelligent Transportation Systems*, vol. 17, no. 10, pp. 2787–2799, 2016.

[9] Y. Yuan, C. X. Wang, X. Cheng, B. Ai, and D. I. Laurenson, "Novel 3D geometry-based stochastic models for non-isotropic MIMO vehicle-to-vehicle channels," *IEEE Transactions on Wireless Communications*, vol. 13, no. 1, pp. 298–309, 2014.

[10] X. Cheng, C.-X. Wang, D. Laurenson, S. Salous, and A. Vasilakos, "An adaptive geometry-based stochastic model for non-isotropic MIMO mobile-to-mobile channels," *IEEE Transactions on Wireless Communications*, vol. 8, no. 9, pp. 4824–4835, 2009.

[11] C.-x. Wang, X. Cheng, and D. Laurenson, "Vehicle-to-vehicle channel modeling and measurements: recent advances and future challenges," *IEEE Communications Magazine*, vol. 47, no. 11, pp. 96–103, 2009.

[12] J. Karedal, F. Tufvesson, N. Czink et al., "A geometry-based stochastic MIMO model for vehicle-to-vehicle communications," *IEEE Transactions on Wireless Communications*, vol. 8, no. 7, pp. 3646–3657, 2009.

[13] A. Borhani and M. Patzold, "Modeling of vehicle-to-vehicle channels in the presence of moving scatterers," in *2012 IEEE Vehicular Technology Conference (VTC Fall)*, pp. 1–5, Quebec City, QC, Canada, 2012.

[14] A. Chelli and M. Patzold, "The impact of fixed and moving scatterers on the statistics of MIMO vehicle-to-vehicle channels," in *VTC Spring 2009 - IEEE 69th Vehicular Technology Conference*, pp. 1–6, Barcelona, Spain, 2009.

[15] M. I. Akram and A. U. H. Sheikh, "On the statistical properties of Nakagami-Hoyt vehicle-to-vehicle fading channel under nonisotropic scattering," *International Journal of Antennas and Propagation*, vol. 2012, Article ID 179378, 12 pages, 2012.

[16] S. Jaeckel, K. Borner, L. Thiele, and V. Jungnickel, "A geometric polarization rotation model for the 3-D spatial channel model," *IEEE Transactions on Antennas and Propagation*, vol. 60, no. 12, pp. 5966–5977, 2012.

[17] 3GPP, "Spatial channel model for multiple input multiple output (MIMO) simulations," Tech. Rep. 3GPP TR 25.996 v10.0.0, European Telecommunications Standards Institute (ETSI), Sophia Antipolis, France, 2011.

[18] Y. Li, R. He, S. Lin et al., "Cluster-based nonstationary channel modeling for vehicle-to-vehicle communications," *IEEE Antennas and Wireless Propagation Letters*, vol. 16, pp. 1419–1422, 2017.

[19] S. Wu, C.-X. Wang, e.-H. M. Aggoune, M. M. Alwakeel, and Y. He, "A non-stationary 3-D wideband twin-cluster model for 5G massive MIMO channels," *IEEE Journal on Selected Areas in Communications*, vol. 32, no. 6, pp. 1207–1218, 2014.

[20] X. Chen, Y. Fang, W. Xiang, and L. Zhou, "Research on spatial channel model for vehicle-to-vehicle communication channel in roadside scattering environment," *International Journal of Antennas and Propagation*, vol. 2017, Article ID 3098198, 12 pages, 2017.

[21] W. Fan, T. Jamsa, J. O. Nielsen, and G. F. Pedersen, "On angular sampling methods for 3-D spatial channel models," *IEEE Antennas and Wireless Propagation Letters*, vol. 14, pp. 531–534, 2015.

[22] N. Avazov and M. Patzold, "A novel wideband MIMO car-to-car channel model based on a geometrical semi-circular tunnel scattering model," *IEEE Transactions on Vehicular Technology*, vol. 65, no. 3, pp. 1070–1082, 2016.

[23] A. Borhani and M. Patzold, "Correlation and spectral properties of vehicle-to-vehicle channels in the presence of moving scatterers," *IEEE Transactions on Vehicular Technology*, vol. 62, no. 9, pp. 4228–4239, 2013.

[24] A. Chelli and M. Patzold, "A wideband multiple-cluster MIMO mobile-to-mobile channel model based on the geometrical street model," in *2008 IEEE 19th International Symposium on Personal, Indoor and Mobile Radio Communications*, pp. 1–8, Cannes, France, 2008.